2023 IEEE International Conference on Robotics and Automation (ICRA 2023)
May 29 - June 2, 2023. London, UK

# Fully Robotized 3D Ultrasound Image Acquisition for Artery

Mingcong Chen, Yuanrui Huang, Jian Chen, Tongxi Zhou, Jiuan Chen and Hongbin Liu, Member, IEEE

***Abstract*— Current imaging of the artery relies primarily on computed tomography angiography (CTA), which requires contrast injections and exposure to radiation. In this paper, we present a method for fully autonomous artery 3D image acquisition using a linear ultrasound (US) probe and a 6 DoFs robot arm with a 3D camera. Robotic vessel acquisition can minimize tissue deformation and permit the reproduction of scans. Additionally, the robotic-based acquisition can provide more precise vessel position data that can be utilized for 3D reconstruction as a preoperative image. The first scanning point is determined by the 3D camera using a neural network for leg area estimation. A visual servo algorithm adjusts the in-plane motions using a cross-sectional vessel segmentation produced by a neural network with a UNet structure, while a US confidence map regulates the in-plane rotation. The robot is equipped with impedance control to maintain a constant and safe scan. Experiments on a leg phantom and a volunteer indicate that the robot can follow the vessel and modify its position to provide a sharper US image. The average error of phantom scanning in y-axis and z-axis are $0.2536mm$ and $0.2928mm$, respectively, while the root means square error (RMSE) of contact force in the volunteer experiment is $0.2664N$. In addition, a 3D vessel reconstruction demonstrates the possibility of robotic US acquisition as a preoperative image.**

## I. INTRODUCTION

The history of ultrasound (US) applications began 1826, when sound waves, known as sonar, were used to detect the distances underwater. In 1942, ultrasonic was initially used as a medical imaging technique in the United States [1]. Ultrasonography is an imaging technique that is non-invasive. Unlike computerized tomography (CT) scans, the patient was not exposed to ionising radiation. In contrast to magnetic resonance imaging (MRI), cardiac pacemakers and metal implants are risk-free for the patient. Ultrasound can detect, localize, and characterize the majority of soft tissue lesions effectively [2]–[4]. Besides locating the lesion and directing the treatment, ultrasonography is a valid imaging method in interventional radiology [5]. The application of ultrasound in the medical and surgical fields encompasses a variety of disciplines, including gynecology and obstetrics, urology, general surgery, and vascular and orthopaedic surgery.

It is well accepted that sonographers have an elevated risk of repetitive strain injury and other musculoskeletal problems associated to their occupation (WRMSDs) [6], [7]. Study conducted with diagnostic medical sonographers and vascular technologists reveal that up to 91% of sonographers report discomfort or pain during ultrasound exams [8]. In several health care departments, ultrasound services have been under growing strain over the past two decades due to the increase in demand and the difficulties in attracting qualified physicians [9]. Automation should be considered in the context of the global shortage of US imaging professionals and the growing demand for ultrasound-based diagnostic imaging. On the other hand, ultrasonography is today a diagnostic technique relayed on experience. Unlike CT, ultrasonic image capture does not have digitalized and standardized regulation. The subjective evaluation of the US scanning process causes the high percentage of missed diagnoses and the difficulties in training new sonographers [10], [11].

Automating diagnosis and intraoperative ultrasound programs guided or assisted by a robot can aid in the resolution of the aforementioned issues by reducing the workload of ultrasound inspectors and laying the foundations for more intelligent image acquisition with a digital and numerical regular [12]. There are currently a number of robotized US scanning systems [13]. In the remote-control ultrasound system, the remote doctor can operate or instruct the robot to acquire US images [14]–[17], which did not address the dearth of ultrasonic specialists. In the 'teach/reply' system, experienced sonographers control the US probe and record the scanning route. The robot system may then automatically execute an ultrasound examination at the patient's location based on the displayed trajectory [18], [19]. Nonetheless, the "teach/reply" technique has limitations when dealing with diverse patients. Visual servo technology enables the robotized system to automatically track the needed image characteristics [20], [21]. P.Chatelain *et al.* [22] implemented confidence map with a visual servo technique. It has been widely employed to prevent US picture shadowing in US robotic systems [23], [24]. Huang et al. suggested a system based on imitation learning for autonomous, completely

Mingcong Chen is with the State Key Laboratory of Management and Control for Complex Systems, Institute of Automation, Chinese Academy of Sciences, Beijing 100190, China, also with the Centre for Artificial Intelligence and Robotics, Hong Kong Institute of Science and Innovation, Chinese Academy of Sciences, Hong Kong mingcong.chen@ia.ac.cn

Yuanrui Huang and Jian Chen are with the School of Artificial Intelligence, University of Chinese Academy of Sciences, Beijing 100049, China chenjian2020@ia.ac.cn huangyuanrui2020@ia.ac.cn

Tongxi Zhou and Jiuan Chen are with the State Key Laboratory of Management and Control for Complex Systems, Institute of Automation, Chinese Academy of Sciences, Beijing 100190, China zhoutongxi2021@ia.ac.cn chenjiuan2021@ia.ac.cn

Hongbin Liu is with the State Key Laboratory of Management and Control for Complex Systems, Institute of Automation, Chinese Academy of Sciences, Beijing 100190, China, also with the Centre for Artificial Intelligence and Robotics, Hong Kong Institute of Science and Innovation, Chinese Academy of Sciences, Hong Kong, and with the School of Biomedical Engineering and Imaging Sciences, King's College London, London SE1 7EU,UK liuhongbin@ia.ac.cn

Corresponding author: Hongbin Liu.

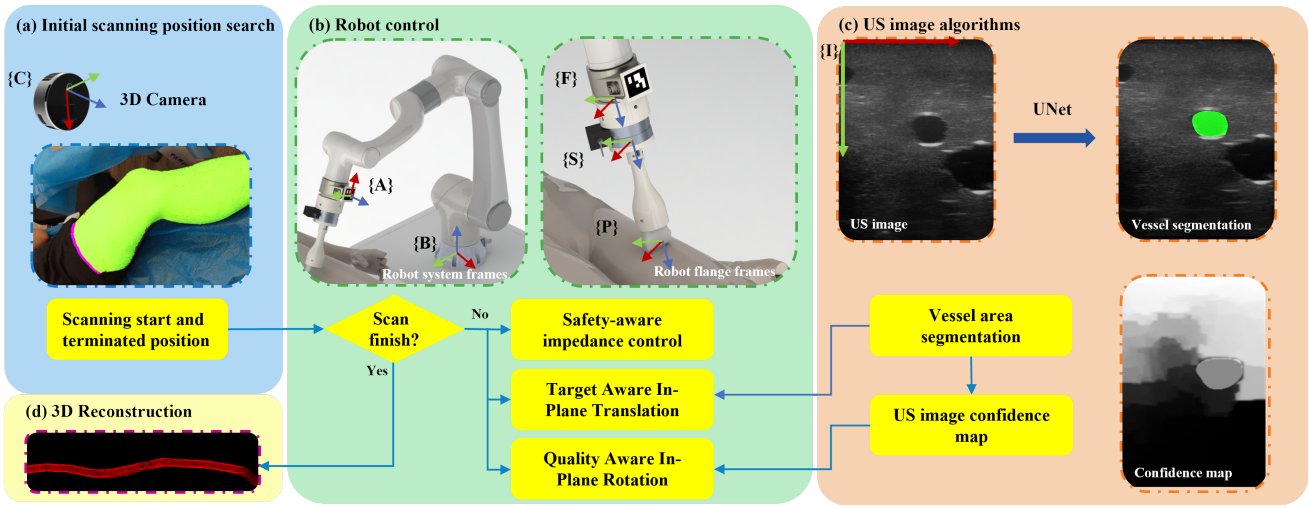


Fig. 1. Overview of the fully robotized ultrasound acquisition system and the system frames (a) initial scanning position search and leg segmentation (b) artery autonomous scanning based on US image image, force sensing and vessel segmentation results (c) vessel cross-section segmentation based on UNet and US image quality evaluation based on US confidence map

automated ultrasonic scanning based on clinical procedures [25]. Jiang et al. demonstrated an end-to-end autonomous robotic sensing system for tubular structures using a neural network for segmentation [26]. A vascularized atlas MRI fro a human arm may be utilized to build a scanning route [27]. However, these systems need a predetermined beginning scanning position or a pre-scanned MRI result.

In this work, we provide a completely autonomous robotic ultrasound system for the artery. A neural network-based leg segmentation and vessel start position search approach are used in the system to determine the start and terminated point of the probe's scanning, allowing the system to adapt to the unique anatomy of each patient. In addition, before training the vessel segmentation UNet [28], an US image data argumentation method is employed to improve the segmentation algorithm adaptability. To guarantee the patient's safety and proper contact, impedance control is utilized. With confidence map-based rotation control and vessel result centring control, the system can reconstruct the vessel structures and follow the artery. Experiments conducted indicate that the system can produce a 3D US image of a human femoral artery.

## II. METHODOLOGY

### A. Overview

The system architecture is depicted in Fig 1. The robot is positioned on the side of the patient's surgery bed, allowing the robot end-effector to easily access the patient's leg. The end-effector of the robot is outfitted with a connector for a 6-axis force sensor that is coupled to a linear US probe. An RGB-D camera placed in front of the operation bed can offer the vessel start position search using a neural network for leg area segmentation in order to direct the US probe to the vascular start point above and provide the scan termination position. As the vessel's depth increasing from the groin to the knee, the scanning will be divided into sections with varying expected contact forces. Once the robot makes contact with the patient and the imaging algorithm identifies the vessel, the robot will proceed from the patient's groin to the knee in order to collect 2D vessel US pictures. During the automated scanning, the probe will compensate for the poor contact between the target leg and US probe, by adjusting the in-plane translation based on real-time vessel position detection from UNet and the in-plane rotation based on the US image confidence map. The scanning technique will utilize an impadence control based on data from a 6-axis force sensor to guarantee patient safety and maintain contact between the US probe and the patient's skin. If the probe reaches the ended location determined by the pre-set scanning length, the scan will terminate and a 3D reconstruction result will be produced.

### B. System Calibration

A fixed ArUco code [29] on the robot end-effector converts the RGB-D camera coordinate to the robot's base coordinate. Consequently, the transformed relationship between RGB-D camera frame $C$ and robot base frame $B$ can be described by ArUco code frame $A$ as the following transform matrix ${}^{C}_{B}T = {}^{F}_{B}T\,{}^{A}_{F}T\,{}^{C}_{A}T$ , where ${}^{j}_{i}T$ is the transformation matrix from frame $i$ to frame $j$.

Additionally, the transform matrix ${}^{I}_{B}T$ should also be calculated to map the position relationship between the US image $I$ and the robot base frame $B$ so that the robotic manipulator can be controlled by the US image. The frames are demonstrated in Fig 1. (b) and the transforming relationship ${}^{I}_{B}T$ can be written as follows

$$ {}^{I}_{B}T = {}^{F}_{B}T\,{}^{S}_{F}T\,{}^{P}_{S}T\,{}^{I}_{P}T \tag{1} $$

where frame $P$ is the US probe frame mount to the connector with a 6-axis force sensor frame $S$ and frame $F$ is the robot flange frame. The robot kinematic model can be calculated from the robot DH parameters, thus the

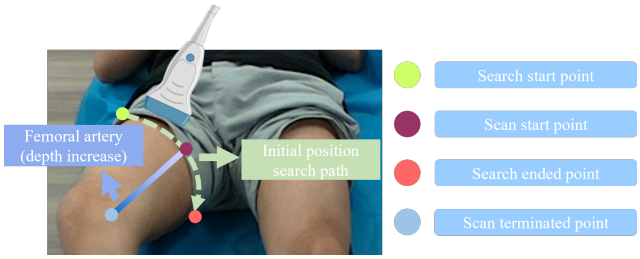


(a)

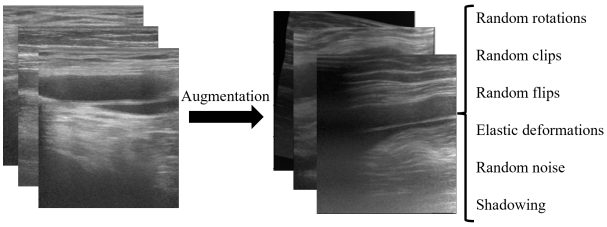


(b)

Fig. 2. (a) Landmarks for femoral artery scanning start point search. (b) US image data augmentation.

transformation ${}^{F}_{B}T$ from the robot flange to the robot base can be obtained by joints' angles from the robot controller API. The force sensor was installed parallel to the robot flange to simplify the calculations of the transformation matrix ${}^{S}_{F}T$. To expand the probe working area on the patient leg, a connector is mounted to the sensor to achieve the transformation ${}^{P}_{S}T$.

For the linear probe, the physical length of the probe transducer $L_T$ obtained from the US machine manufacturer will influence the US image elements. The image depth $D_I$ set on the US machine can map the relationship between physical length $(x_P, y_p)$ and the US Image pixel $(x, y)$ as $(x_P, y_p) = (\frac{L_T}{W_x}, \frac{D_I}{H_y})$ where $W$ is the US image pixel width and $H$ is the US image pixel height. Hence, the transformation matrix ${}^{I}_{P}T$ can be described as follows

$$\begin{bmatrix} \frac{L_T}{W} & 0 & 0 & \frac{L_T}{2} \\ 0 & \frac{D_I}{H} & 0 & D_I \\ 0 & 0 & 1 & 0 \\ 0 & 0 & 0 & 1 \end{bmatrix} \tag{2}$$

### C. Femoral Artery Start Position Search

The surface marking of the femoral artery is represented by the upper two-thirds of a line joining the mid-inguinal point (midway between the anterior superior iliac spine and the pubic symphysis), to the adductor tubercle, with the thigh abducted and rotated outward [30]. In our approch, a segmentation network whose backbone is UNet is trained to locate the leg area, which is demenstrated in Fig 1(a). As Fig 2(a) shows, the upper boundary of the segmentation result is set as the US probe searching path, which is the trajectory from anterior superior iliac spine to public symphysis. In addition, matching the depth pictures with the RGB images using calibration approach as (1), the pixel coordinates of the initial searching landmarks identified by the approch are transfered to the robot's base coordinate. The robot can reach the start point and search the vessel in the defined searching path, once the vessel is tracked the search procedure will terminate and perform the US image acquisition. The scanning length in the system is pre-set by the doctors then the terminated position can be generated. As the femoris artery passes through the adductor canal and changes into to the popliteal artery, the vessel's distance from the skin increasing [31] should lead the expected contact force increase in the system.

### D. Target Aware In-Plane Translation

U-Net is a convolutional neural network created specifically for biomedical image segmentation, which based on a fully convolutional network that has been tweaked and expanded to accommodate less training pictures [28]. As the cross-section view contains vessel location information, the U-Net requires a collection of vessel cross-section photos as training data. In order to suit for the complicated US data collecting and the different picture alterations, it is important to enrich the data prior to training. As illustrated in Fig 2.(b) data augmentation method is employed in our approach to generate random elastic deformation and random shadow. The elastic deformation resembles the vascular structure that is compressed by the US probe. The US image shadowing approach is presented to improve the capability of vessel segmentation under inadequate probe-skin coupling. Once a model has been trained, it is able to segment the vascular cross-section from the US image under varied contact pressures and probe in-plane rotations. The area of vessel part is illustrated in white in the resulting mask whose weight of centre can be calculated by image moments as

$$\bar{x} = \frac{\sum_x \sum_y S(x,y) \cdot x}{\sum_y \sum_y S(x,y) \cdot x \cdot y} \tag{3}$$

where $S(x, y)$ is the grey value of the segmentation result image in row y and col $x$.$\bar{x}$ is the vessel weight centre coordinates in the transducer x-axis. Hence, we can calculate the in-plane translation velocity as

$$v_x = \eta \bar{x} \tag{4}$$

where $\eta > 0$ is the control gain.

### E. Quality Aware In-Plane Rotation

Confidence map is a way for evaluating the US image quality. It is capable of describing the image quality of each pixel. Each grayscale original US image $G(x, y) \in [0, 1]$can be represented in the confidence map $C(x, y) \in [0, 1]$ as the confidence of a US acquisition in that pixel $G(x, y)$. The probability that each pixel $(x, y)$ the virtual transducer is determined by random walk in the confidence map [32].The top row of the US picture is labeled with a 1 for confidence, while the bottom row is labeled with a 0. The US picture is attenuated based on the depth of the US signal transduced prior to the random walk computation. The probe's angle of contact with the skin may be determined using the confidence map. Calculating the confidence map by setting up the

picture as an 8-connected lattice graph with connection weights based on the grey value similarity of neighboring pixels will result in low confidence in the vessel area, whose expression in the US image is dark. The U-Net segmentation mask is blended with the confidence map to resolve the low confidence in the vessel region.

The distribution in the x-axis of the confidence map can be calculated by the 1st moment as

$$M_x = \frac{\sum_x \sum_y C'(x,y) \cdot x}{\sum_x \sum_y C'(x,y)} \tag{5}$$

where $C'(x,y)$ is the merged confidence of pixel $(x,y)$, and when $M_x = 0$ corresponds to the central scan line of the US image. To compensate for the shadow in US image caused by the air between the probe and the patient's skin, the geometric feature can also be described as an in-plane rotation angle as

$$\omega = a(F) \cdot M_x \tag{6}$$

a sigmoid activation function $a(F)$ is to ensure that only apply in-plane rotation control when the probe has proper contact with the skin. $F_e$ is expected contact force between the probe and target skin.

$$a(F) = \begin{cases} 0 & F \leq 1N \\ \frac{1}{1+e^{\frac{1}{F-F_e} - \frac{1}{F_e - F}}} & 1N < F < F_e \\ 1 & F \geq F_e \end{cases} \tag{7}$$

### F. Safety Aware Impedance Control

Contact force is one of the key parameters in ultrasound acquisition, which the robot must maintain a constant force between the probe and target skin to ensure the patient's safety and the US image quality. It is necessary to calibrate the probe weight centre $G$ and initial value $F_0$ of the force sensor. Hence, the contact force from the probe can be described as

$$F = F_S = F_0 - {}^S_B R^{-1} G \tag{8}$$

where $F_S$ is real-time data read from the force sensor and ${}^S_B R^{-1}$ is the rotation matrix from robot base frame $B$ to sensor frame $S$. The control signal for the robot arm joints is expressed as

$$\Delta q = (\mathbf{J^T(q)J(q)} + \lambda^2 \mathbf{I})^{-1} \mathbf{J^T(q)e} \tag{9}$$

in which $\mathbf{q}$ is the robot joint vector, $J(\mathbf{q})$ is the robot Jacobian matrix and $\lambda$ is a non-zero damping constant. $\mathbf{e}$ is the difference between the probe current position and target position in robot base frame, which is $\mathbf{e} = [\mathbf{v_x} \quad \mathbf{v_y} \quad \mathbf{v_z} \quad \omega \quad \mathbf{0} \quad \mathbf{0}]$.An impedance controller is employed in the system to illustrate $v_z$ as

$$v_z = v_{z0} t + \frac{t M^{-1} (F - F_e - D v_{z0})}{2} \tag{10}$$

where $v_{z0}$ is the current robot joints velocity, $t$ is the robot controller servo time. $M$ and $D$ are the mass and damping elements for the impedance controller respectively.

TABLE I
VESSEL SEGMENTATION UNET PERFORMANCE WITH DIFFERENT DATA AUGMENTATION SETTING

| Method | Operations | DICE |
|---|---|---|
| No augmentation | | 42.659% |
| Augmentation | Random crop, rotation, noise | 86.981% |
| Augmentation | Random crop, rotation, noise, shadow, elastic deformation | 92.624% |

## III. EXPERIMENTS

### A. Experimental Setup

The experiment setup can be seen from Fig 4. (a). The robot employed in our experiments is a collaborative robot with 6 DoFs (Elfin 5kg, Han's Robot, China). The robot is attached with a six-axis force sensor (M3815D, Sunrise Instruments, China) and carries a liner US probe (Pionner H20, Angell, China). Between the robot end-effector and the force sensor, an ArUco-mark 3D-printed connector is mounted. Using a stream capture device (Pro Capture, Magewll, China), the $38 \times 50mm$ real-time US picture is formatted as a $400 \times 600$ pixel image and delivered to the workstation. A 3D camera (RealSense L515, Intel, USA) is positioned in front of the patient bed to capture the human and estimate the anatomy and offer the transformation between the target and ArUco mark.

Two experiments are included in this section. One demonstrates the accuracy and stability of the proposed control system by semi-automatically scanning a femoral vascular access ultrasound phantom (Blue Phantom, CAE Healthcare, USA) without anatomy estimate. Another experiment is a totally automated US image capture experiment on a volunteer.

### B. Vessel Segmentation Performance

Five participants and the femoral vascular access phantom provided a total of 500 training US image datasets. The approach is an online dataset enhancement, and the image will be created randomly when loaded into the training network. Dice coefficient $s = \frac{2|X+Y|}{|X|+|Y|}$ was used to assess the proposed data augmentation approach in this study. The loss function and optimiser employed were $\varsigma = 1 - s$ and root mean square propagation (RMSprop). The learning rate was 0.001. The model was trained on a workstation (Dell, Nvidia RTX3090Ti). The result of training is shown in Table 1., in which the epoch was set as 100 and the validation percentage is $2\%$.

### C. Phantom Experiment

The leg phantom was placed in a water-filled container along the x-axis of the robot's base frame, and the probe was manually placed in water above the beginning of the vessel, but without contacting leg phantom. The probe was controlled by $moveL()$ command to scan a $140mm$ vessel with 1mm gap along the x-axis, which can extract the vessel centre towards the vessel direction by OpenCV with a grey value threshold algorithm. The recorded vessel center location can be regarded as the true 3D trajectory of the

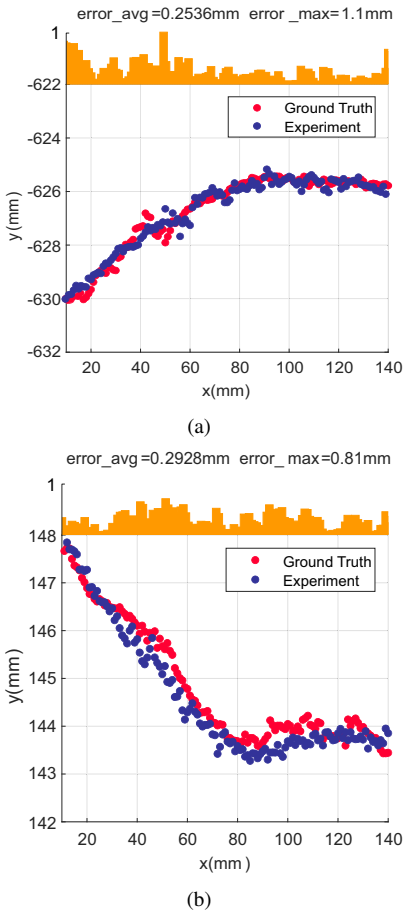


Fig. 3. (a) The vessel center trajectory in robot base frame X-Y axis. The difference of y-axis in every single value in x-axis is the orange bar above the trajectory scatter graph. (b) The vessel center trajectory in robot base frame X-Z axis. The difference of z-axis in every single value in x-axis is the orange bar above the trajectory scatter graph

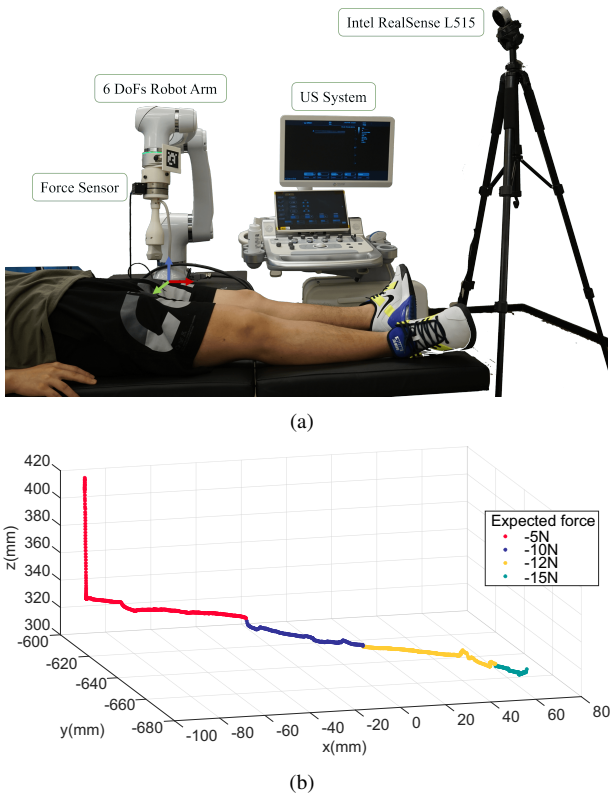


Fig. 4. (a) Physical setup of the experiment on volunteer (b) The recorded probe trajectory of volunteer experiment. The trajectory is separated into four sections by setting different expected contact force in 5N, 10N, 12N and 15N

phantom vessel. Without moving the phantom, emptied the experiment container of water and performed the system control algorithm with the same starting and ending positions as the ground truth. The system may change the probe's rotation to establish a suitable contact with the leg and move the probe along the robot base frame's y-axis to maintain the vessel's center in alignment with the probe's center scan line. The vessel centre was the weight centre of the UNet based vessel segmentation area. $\eta = 0.01$ is the control gain parameter, and $F_e = 3N$ is the estimated force required to maintain a satisfactory US picture for the phantom. The vessel center was transformed from US image coordinates to the robot arm base coordinates in order to examine the disparity between the ground truth and the experiment outcome.

It is noticeable that these two trajectories have the same trend, and each point on the same x value has a similar value on the y- and z-axes of the robot's base frame. Fig. 3. (a) depicts the y-axis distribution of the vessel center along the x-axis. The ground truth and experiment results are very consistent, with an average error of $0.2536mm$ and a maximum difference of 1.1mm in the $140mm$ scanning. As shown in Fig. 3. (b), the average error of the vessel center along the z-axis is $0.2928mm$ and the highest error is only $0.81mm$. Both the y-axis and z-axis differences between the two trajectories are less than 3 pixels and 4 pixels, which should be produced by pixels damping from vessel area selection by threshold algorithm or UNet as a result of the phantom manufacturing mistake.

### *D. Volunteer Experiment*

In this study, we collected a dataset from eight volunteers with diverse leg positions in bed to train the leg segmentation neural network. The anatomy estimate method generates the scanning trajectory, which is divided into four sections with varying expected forces of $-5N$, $-10N$, $-12N$ and $-15N$. The impedance control mass and damping parameters are set as 7 and 20, respectively, while the non-zero dump constant is set to $\lambda = 0.01$. The system effectively located the authorized artery initial point and tracked the vessel while maintaining adequate contact and US image quality. The scanning for the volunteer's femoral artery is totally automated and was performed six times after US gel was applied to the skin of the volunteer. Fig 4. (b) illustrates the recorded probe path of one experiment involving the volunteer. The scanning path covered a 160mm long vessel area and the four force section's demarcations are $100mm$, $150mm$ and $200mm$.

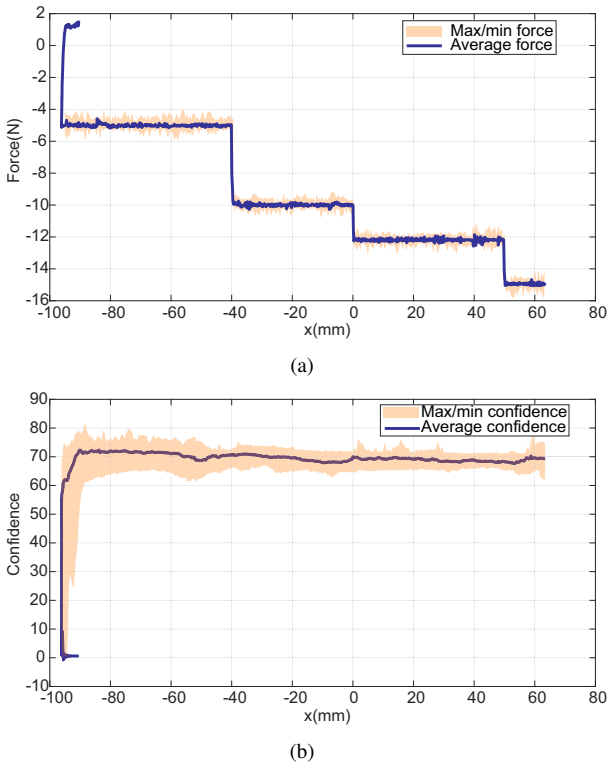


Fig. 5. (a) The average force of six times volunteer experiments. The transparent region is the maximum and minimum force value in each step. (b) The average mean confidence of six times volunteer experiments. The transparent region is the maximum and minimum mean confidence value in each step

Fig 5. (a) demonstrates that the probe makes contact with the target skin and maintains the predicted force in accordance with the results of the scanning start position estimation. The average contact force in the three rounds experiment is stable at each target value with a $\pm 1N$ damping, whose root mean square values are $-5.014N$, $-9.978N$, $-12.19N$ and $-14.905N$. The root means square error (RMSE) of force under contact conditions is $0.2664N$. The variance of contact force during the entire scanning procedure is $2.7235$ and after contacting the value of variance was reduced to $0.071$. It is easy to see the contact is very stable with the system proposed control logic.

Fig 5. (b) shows the mean confidence $\bar{C} = \frac{\sum_x \sum_y C'(x,y)}{xy}$ during the US image acquisition of three times. It is noticeable that the confidence keeps a high level after contact with the target skin, and the mean value of it is $69.41$ after stable contact. The 3D structure of vessel reconstructed in this work is shown in the submitted video.

## IV. Discussion

This study proposed a fully automatic femoral artery acquisition system. The method permits the robotic US scanning system to execute the diagnostic without human intervention. In contrast to the semi-automatic robotic US system, in which the US probe must be manually moved to its beginning location, our study demonstrates how an autonomous estimation method directed the US probe to its initial and final scanning positions. Significantly, the force modification based on anatomy may accommodate the variation in vessel depth from the skin. Our results also show how an US image data argumentation approach increases the accuracy of segmentation with a tiny dataset. With the segmentation results, the scheme shows how to maintain the vessel by in-plane translation over the US probe's centre scan line. Our results for in-plane rotation control illustrate the use of the US confidence map to compensate the air between the US probe and the target skin. In addition, the weighted segmentation result can also be utilized to address the low confidence in vessel area, hence resolving the unexpected rotation when the probe is placed upon the vessel. Our system includes impedance control to ensure the safety of patients. During the volunteer experiment, our study constructed a 3D image of the femoral artery based on the results of vessel segmentation and multiple frame transformation.

However, the scanning start position estimation only performs a lead for the probe to find the initial scanning position. Although the robot can maintain the position of the target at the centre scan line, once it finds the target by the proposed target aware in-plane translation, the system still faces the mistracking of the vessel. A more detailed guide is necessary for the system, such as generating the trajectory of the vessel based on the priority of anatomy. Due to the lack of CT data of phantom and volunteers, there are no 3D result registrations and evaluations in our experiments. For the femoral artery, the depth of it increases along the leg direction from the groin to the knee. A defined force impedance control cannot keep visualising the vessel during the whole scanning procedure, so an adapted force control based on the anatomy trajectory will be necessary. Reinforcement learning technology is an effective method for locating the expected US image acquisition. Moreover, the UNet structured vessel segmentation method cannot handle the various clinical conditions, especially distinguish the anatomy of artery and vein. Alternatively, a multi-modular recurrent network with US visual information and force sensor haptic information can be further integrated to discriminate vessel types, which is imitating the doctor separate artery and vein by applying pressure to the vascular structure.

## V. Conclusion

In this work, we proposed a fully automatic femoral artery 3D ultrasound acquisition system. Without any pre-operation, the proposed method can identify the vessel's initial location. The system can also tune the contact force to get the deeper artery under the skin based on pre-set scanning distance. It can also adapt the probe to maintain the vessel in the center of the image based on segmentation results and control the probe's rotation to match the curvature of the thigh. This strategy has the potential to digitalize and standardize the US image procurement. The system is only presented for the femoral artery scanning, but it is also customizable enough to be suitable for other applications.

## REFERENCES


[1] K. F. Graff, "A history of ultrasonics," in *Physical acoustics*. Elsevier, 1981, vol. 15, pp. 1–97.

[2] S. Sintzoff Jr, I. Gillard, D. Van Gansbeke, P.-A. Gevenois, I. Salmon, and J. Struyven, "Ultrasound evaluation of soft tissue tumors." *Journal belge de radiologie*, vol. 75, no. 4, pp. 276–280, 1992.

[3] É. Cardinal, C. G. Beauregard, and R. K. Chhem, "Interventional musculoskeletal ultrasound," in *Seminars in Musculoskeletal Radiology*, vol. 1, no. 02. © 1997 by Thieme Medical Publishers, Inc., 1997, pp. 311–318.

[4] É. Cardinal, R. K. Chhem, and C. G. Beauregard, "Ultrasound-guided interventional procedures in the musculoskeletal system," *Radiologic clinics of North America*, vol. 36, no. 3, pp. 597–604, 1998.

[5] J. Del Cura, R. Zabala, and I. Corta, "Ultrasound-guided interventional procedures in the musculoskeletal system," *Radiología (English Edition)*, vol. 52, no. 6, pp. 525–533, 2010.

[6] E. Seto and L. Biclar, "Ambidextrous sonographic scanning to reduce sonographer repetitive strain injury," *Journal of Diagnostic Medical Sonography*, vol. 24, no. 3, pp. 127–135, 2008.

[7] G. Harrison and A. Harris, "Work-related musculoskeletal disorders in ultrasound: Can you reduce risk?" *Ultrasound*, vol. 23, no. 4, pp. 224–230, 2015.

[8] K. Evans, S. Roll, and J. Baker, "Work-related musculoskeletal disorders (wrmsd) among registered diagnostic medical sonographers and vascular technologists: a representative sample," *Journal of Diagnostic Medical Sonography*, vol. 25, no. 6, pp. 287–299, 2009.

[9] L. Waring, P. K. Miller, C. Sloane, and G. Bolton, "Charting the practical dimensions of understaffing from a managerial perspective: The everyday shape of the uk's sonographer shortage," *Ultrasound*, vol. 26, no. 4, pp. 206–213, 2018.

[10] Y. Zhang, H. Xia, Y. Wang, L. Chen, S. Li, I. A. Hussein, Y. Wu, Y. Shang, S. Yao, and R. Du, "The rate of missed diagnosis of lower-limb dvt by ultrasound amounts to 50% or so in patients without symptoms of dvt: A meta-analysis," *Medicine*, vol. 98, no. 37, 2019.

[11] D. J. Blehar, B. Barton, and R. J. Gaspari, "Learning curves in emergency ultrasound education," *Academic emergency medicine*, vol. 22, no. 5, pp. 574–582, 2015.

[12] D. R. Swerdlow, K. Cleary, E. Wilson, B. Azizi-Koutenaei, and R. Monfaredi, "Robotic arm–assisted sonography: Review of technical developments and potential clinical applications," *American Journal of Roentgenology*, vol. 208, no. 4, pp. 733–738, 2017.

[13] K. Li, Y. Xu, and M. Q.-H. Meng, "An overview of systems and techniques for autonomous robotic ultrasound acquisitions," *IEEE Transactions on Medical Robotics and Bionics*, vol. 3, no. 2, pp. 510–524, 2021.

[14] M.-A. Janvier, L.-G. Durand, M.-H. R. Cardinal, I. Renaud, B. Chayer, P. Bigras, J. De Guise, G. Soulez, and G. Cloutier, "Performance evaluation of a medical robotic 3d-ultrasound imaging system," *Medical image analysis*, vol. 12, no. 3, pp. 275–290, 2008.

[15] T. Essomba, L. Nouaille, M. Laribi, G. Poisson, and S. Zeghloul, "Design process of a robotized tele-echography system," in *Applied Mechanics and Materials*, vol. 162. Trans Tech Publ, 2012, pp. 384–393.

[16] A. Rykkje, J. F. Carlsen, and M. B. Nielsen, "Hand-held ultrasound devices compared with high-end ultrasound systems: a systematic review," *Diagnostics*, vol. 9, no. 2, p. 61, 2019.

[17] R. Monfaredi, E. Wilson, B. Azizi koutenaei, B. Labrecque, K. Leroy, J. Goldie, E. Louis, D. Swerdlow, and K. Cleary, "Robot-assisted ultrasound imaging: Overview and development of a parallel telerobotic system," *Minimally Invasive Therapy & Allied Technologies*, vol. 24, no. 1, pp. 54–62, 2015.

[18] G. P. Mylonas, P. Giataganas, M. Chaudery, V. Vitiello, A. Darzi, and G.-Z. Yang, "Autonomous efast ultrasound scanning by a robotic manipulator using learning from demonstrations," in *2013 IEEE/RSJ International Conference on Intelligent Robots and Systems*. IEEE, 2013, pp. 3251–3256.

[19] M. Victorova, D. Navarro-Alarcon, and Y.-P. Zheng, "3d ultrasound imaging of scoliosis with force-sensitive robotic scanning," in *2019 third IEEE international conference on robotic computing (IRC)*. IEEE, 2019, pp. 262–265.

[20] Z. Cui, W. Li, X. Zhang, P. W. Y. Chiu, and Z. Li, "Accelerated dual neural network controller for visual servoing of flexible endoscopic robot with tracking error, joint motion, and rcm constraints," *IEEE Transactions on Industrial Electronics*, vol. 69, no. 9, pp. 9246–9257, 2022.

[21] Z. Cui, J. Li, W. Li, X. Zhang, P. W. Y. Chiu, and Z. Li, "Fast convergent antinoise dual neural network controller with adaptive gain for flexible endoscope robots," *IEEE Transactions on Neural Networks and Learning Systems*, pp. 1–14, 2022.

[22] P. Chatelain, A. Krupa, and N. Navab, "Optimization of ultrasound image quality via visual servoing," in *2015 IEEE international conference on robotics and automation (ICRA)*. IEEE, 2015, pp. 5997–6002.

[23] M. K. Welleweerd, A. G. de Groot, S. de Looijer, F. J. Siepel, and S. Stramigioli, "Automated robotic breast ultrasound acquisition using ultrasound feedback," in *2020 IEEE International Conference on Robotics and Automation (ICRA)*. IEEE, 2020, pp. 9946–9952.

[24] K. Li, J. Wang, Y. Xu, H. Qin, D. Liu, L. Liu, and M. Q.-H. Meng, "Autonomous navigation of an ultrasound probe towards standard scan planes with deep reinforcement learning," in *2021 IEEE International Conference on Robotics and Automation (ICRA)*. IEEE, 2021, pp. 8302–8308.

[25] Y. Huang, W. Xiao, C. Wang, H. Liu, R. Huang, and Z. Sun, "Towards fully autonomous ultrasound scanning robot with imitation learning based on clinical protocols," *IEEE Robotics and Automation Letters*, vol. 6, no. 2, pp. 3671–3678, 2021.

[26] Z. Jiang, Z. Li, M. Grimm, M. Zhou, M. Esposito, W. Wein, W. Stechele, T. Wendler, and N. Navab, "Autonomous robotic screening of tubular structures based only on real-time ultrasound imaging feedback," *IEEE Transactions on Industrial Electronics*, vol. 69, no. 7, pp. 7064–7075, 2021.

[27] Z. Jiang, Y. Gao, L. Xie, and N. Navab, "Towards autonomous atlas-based ultrasound acquisitions in presence of articulated motion," *IEEE Robotics and Automation Letters*, 2022.

[28] O. Ronneberger, P. Fischer, and T. Brox, "U-net: Convolutional networks for biomedical image segmentation," in *International Conference on Medical image computing and computer-assisted intervention*. Springer, 2015, pp. 234–241.

[29] S. Garrido-Jurado, R. Muñoz-Salinas, F. J. Madrid-Cuevas, and M. J. Marín-Jiménez, "Automatic generation and detection of highly reliable fiducial markers under occlusion," *Pattern Recognition*, vol. 47, no. 6, pp. 2280–2292, 2014.

[30] H. Gray, *Anatomy, descriptive and applied*. Lea & Febiger, 1910.

[31] P. D. Garrett, R. E. Eckart, T. D. Bauch, C. M. Thompson, and K. C. Stajduhar, "Fluoroscopic localization of the femoral head as a landmark for common femoral artery cannulation," *Catheterization and cardiovascular interventions*, vol. 65, no. 2, pp. 205–207, 2005.

[32] A. Karamalis, W. Wein, T. Klein, and N. Navab, "Ultrasound confidence maps using random walks," *Medical image analysis*, vol. 16, no. 6, pp. 1101–1112, 2012.